Repeat-Pass Dual-Antenna Synthetic Aperture Radar Interferometric Change-Detection Post-Processing

David A. Yocky and Benjamin F. Johnson

Abstract

Synthetic aperture radar (SAR) interferometric change-detection (ICD) maps are highly sensitive to both macro and micro temporal changes in SAR surface reflectivity. This change is detected as decorrelations in the complex cross-correlation between two SAR complex images collected at different times. However, in many instances, numerous detected decorrelations are not due to changes during the elapsed time, but due to other decorrelating effects. Using information from a repeat-pass, dual-antenna interferometric SAR (IFSAR) change pair, we were able to identify over 70 percent of the ICD correlations less than 0.80 as non-temporal changes, or false changes. The remaining temporal changes coincided well with controlled changes made in the scene. Our post-processing results show the IFSAR coherence maps to be the most informative SAR data component for such false temporal change analysis.

Introduction

Conventional synthetic aperture radars (SAR) are active microwave systems usually operating in the 250-MHz to 50-GHz range. The radiation, emitted and then scattered back to the radar, is captured as complex imagery (wavefront) data containing both amplitude and phase information. Given a time lapse and precise repeat collection geometry, SAR datasets can be compared in a coherent manner, i.e., combining wavefront data using complex arithmetic. This provides the opportunity to create interferometric change detection pairs.

Interferometric change detection (ICD) compares complex reflection between SAR image pairs by using complex cross-correlation measures. The change (decorrelation) that is detected is influenced by both amplitude and phase changes, making it more sensitive than incoherent change detection (Gabriel *et al.*, 1989; Zebker and Villasenor, 1992; Massonnet *et al.*, 1993; Eichel *et al.*, 1996; Jakowatz *et al.*, 1996). However, in many instances, numerous changes are not temporal in nature but are due to other effects. Zebker and Villasenor (1992) identified some of these decorrelation sources for dual-pass radar interferometry and showed the utility of correcting these for deriving terrain maps. In this paper, we apply these corrections and others to the ICD map, post-processing for false change identification. We use a high-resolution (0.37-m) dual-antenna airborne interferometric SAR (IFSAR) in a repeat-pass mode to collect temporal change-detection pairs. We show the added utility of using IFSAR versus just dual-pass SAR data in ICD post-processing. We use SAR-derived signal-to-noise, magnitude change, and height data, and IFSAR-derived coherence for identifying non-temporal changes and refining the final ICD map.

SAR Interferometric Change Detection

The emitted electromagnetic wave from a SAR scatters off a given real target, altering the amplitude and phase (and polarization) of the original signal. This reflected signal gives information such as surface roughness, reflectivity, shape, size, and dielectric constant. The collected return signal is processed to reconstruct the scattering phenomena as a complex image. The magnitude of the complex image is the "detected" or "intensity" image.

If a target is imaged twice, given a time lapse and the same collection geometry, the target complex reflectivity can vary due to position or surface property change. Signal similarity between passes is expressed by the correlation estimate given by

$$\gamma = \frac{\left|\sum_i \sum_j g_{ij}^* \cdot h_{ij}\right|}{\sqrt{\sum_i \sum_j |g_{ij}|^2 \cdot \sum_i \sum_j |h_{ij}|^2}} \quad (1)$$

where g_{ij} is the first registered complex image, h_{ij} is the second registered complex image, both for the ith range index and the jth azimuth index, and the summation is over the number of complex looks. A totally correlated pair of images would be a matrix of ones while any decorrelation would be values less than unity. The correlation given by Equation 1 is also called coherence because it is analogous to the optical complex coherence factor (Goodman, 1985). We use the terms correlation and coherence to denote the dual-pass and single-pass dual-antenna quantities of Equation 1, respectively.

Jakowatz *et al.* (1996) has shown that the maximum-likelihood temporal change estimator, $\hat{\gamma}_{ml}$, of SAR reflectance with additive Gaussian noise is

$$\hat{\gamma}_{ml} = \frac{2\left|\sum_i \sum_j g_{ij}^* \cdot h_{ij}\right|}{\sum_i \sum_j |g_{ij}|^2 + \sum_i \sum_j |h_{ij}|^2} \quad (2)$$

where g and h are those of Equation 1. This derivation assumes that images g and h have the same average clutter power. While Equation 2 is similar to Equation 1, the denominators are the arithmetic and geometric means, respec-

Systems Analysis Department II, Sandia National Laboratories, P.O. Box 5800, Albuquerque, NM 87185-0572 (dayocky@sandia.gov).

Photogrammetric Engineering & Remote Sensing, Vol. 64, No. 5, May 1998, pp. 425–429.

0099-1112/98/6405–425$3.00/0

tively. The image power assumption in deriving Equation 2 results in the maximum-likelihood estimator being less than unity for the case of image power variation with no SAR reflectance change. This is significant because operational SAR illuminating power can vary from day to day or even pass to pass. Because we are interested in the change in complex SAR reflectance from one pass to another, change due to illuminating power differences is undesirable. Using the geometric mean and subsequent estimator, Equation 1, accommodates this, i.e., $\hat{\gamma}_{ml} = 0.8$ and $\gamma = 1.0$ for $g = 0.5h$.

Equation 1 indicates that decorrelation,$1 - \gamma$, is both amplitude and/or phase difference dependent. Processing two complex SAR images from two identical collection-geometry flights (repeat-pass) with Equation 1 produces an ICD map. The change detection captured by the correlation measure embodies high change sensitivity for both macro, i.e., cars present in one pass and absent in another, and micro, i.e., rocks moved by a human walking on them, changes. Many smaller changes are not obvious by doing just SAR intensity imagery comparisons, but are captured by the phase change in the objects or surface. The final correlation value produced in the ICD calculation is a quantitative measure of the amount of change. The ICD map, being the correlation map, provides both spatial location and magnitude values for apparent SAR complex reflectance change between passes. Researchers at Sandia National Laboratories (SNL) have automated and shown the utility of the dual-pass SAR ICD processes (Eichel *et al.*, 1996; Jakowatz *et al.*, 1996).

Numerous factors contribute to the correlation in Equation 1 other than temporal changes in the SAR complex reflectance. The contributing sources can be represented as

$$|\gamma| = |\gamma_{\text{temporal}}| \cdot |\gamma_{\text{thermal}}| \cdot |\gamma_{\text{registration}}| \cdot |\gamma_{\text{spatial}}| \tag{3}$$

after Bickel and Hensley (1996) where γ is that in Equation 1, γ_{temporal} is the correlation due to target position or surface reflectance change, γ_{thermal} is the correlation due to thermal noise, $\gamma_{\text{registration}}$ is the correlation due to registration, and γ_{spatial} is the correlation due to antenna separation and target type. The temporal component is of interest for ICD. Thus, if the other components can be measured, estimated, or identified, the decorrelation due only to temporal change can be found.

Thermal noise is produced by antenna, receiver, and system electronics, as well as blackbody radiation sources in the scene. Thermal correlation can be represented as

$$\gamma_{\text{thermal}} = \sqrt{\left(\frac{1}{1 + \text{SNR}_1^{-1}}\right) \cdot \left(\frac{1}{1 + \text{SNR}_2^{-1}}\right)} \tag{4}$$

where SNR is the signal-to-noise ratio, and the indices denote the two images (Zebker and Villasenor, 1992). Low SNR will cause decorrelation.

The registration correlation is dependent on precise registration of impulse responses between image pairs and is critical in correlating pixels between images. SNL automated ICD image pair registration which minimizes the $\gamma_{\text{registration}}$ decorrelation for slowly undulating terrain. This registration is done by dividing the complex imagery into power-of-2 patches and performing cross-correlations between image patches using Fourier multiplication. The cross-correlation peak location and strength is used to select tie-points and calculate global or local warping functions. More detail is found in Jakowatz *et al.* (1996; chapter five).

γ_{spatial} is dependent on the local terrain and scattering properties of the imaged target. It can be represented as having two contributions. One is the geometric correlation, which Prati (1989) and Bickel and Hensley (1996) have presented in previous work, accounting for local terrain slope. For a rectangular SAR impulse response, the range correlation can be expressed as

$$\gamma_{\text{geometry}} = \left|\text{sinc}\left[\frac{2}{\lambda}\rho_r \tan(\phi + \alpha)\,\Delta\phi\right]\right| \tag{5}$$

where $\text{sinc}(x) = \sin\pi x/\pi x$, λ is the SAR wavelength, ρ_r is the range resolution, ϕ is the depression angle ($0 \le \phi \le 90$), α is the local slope angle, and $\Delta\phi$ is the change in depression angle for the two passes. The correlation is dependent on the local slope component perpendicular to the baseline normal. The other spatial component, γ_{volume}, is due to volume scatterers in the scene. The volume scattering decorrelation is caused by the increased spatial extent and penetration of the SAR returns (Rodriguez and Martin, 1992; Gray and Farris-Manning, 1993; Askne *et al.*, 1997).

Coherence

The mathematical expression for IFSAR coherence is identical to Equation 1, except that the two complex signals are simultaneously collected on separate antennas. Likewise, the coherence can be expressed as a product of coherence components

$$|\gamma_{\text{coherence}}| = |\gamma'_{\text{thermal}}| \cdot |\gamma'_{\text{registration}}| \cdot |\gamma'_{\text{spatial}}|, \tag{6}$$

the primes indicating a single-pass, dual-antenna measurement. We have assumed that the temporal change over an aperture is negligible. This is a good assumption for a calm day with no moving vehicles in the scene. Targets with low coherence may include large terrain slope, volume scatterers (i.e., tree canopies), and buildings.

The registration between single-pass channels is well-controlled and the coherence degradation is minimal for the SNL IFSAR configuration. The right-hand side of Equation 6 is then only the thermal and spatial components. The single-pass thermal coherence contributions are

$$\gamma'_{\text{thermal}} = \frac{1}{1 + \text{SNR}_n^{-1}} \tag{7}$$

where n is number of the pass. For the dual-pass case ($n = 1, 2$), these are the individual thermal components in Equation 4. The single-pass spatial coherence component is dependent on the two-antenna geometry and target type. We don't separate the single-pass thermal and spatial components in our use of the coherence.

False-Change Identification

The above discussion illustrates that dual-pass correlation is a product of many components, some of which are not temporal decorrelation. Temporal changes being of interest, all other changes are false temporal changes. Reduction of false-change signals enhances the interpretability of the final product.

Change-detection pairs of SNL's Exterior Intrusion Sensor Facility (EISF) were collected on 16 May 1996 using the Department of Energy's P-3 Orion-based Airborne Multisensor Pod System (AMPS) dual-antenna K_u-band (15 GHz) IFSAR system at 0.37-m ground resolution, 6.5-km nominal slant range, and a 35° antenna depression angle. The IFSAR was designed by SNL with a 0.374-m baseline. The P-3 flew multiple flights over the EISF from east to west. We selected two dual-antenna IFSAR passes with a 40-minute time lapse between collections. The dual-pass baseline was calculated to be about 7.5 m.

During the time between passes, controlled changes were made in and around the EISF; that is, human traffic, walking, outlined geometric shapes in the EISF gravel, and an arrow in the dirt outside the EISF fence. There was light vehicle traffic in the dirt around the fences.

Figure 1 is a digitized photograph of the L-shaped, fence-enclosed EISF and surrounding facilities at approxi-

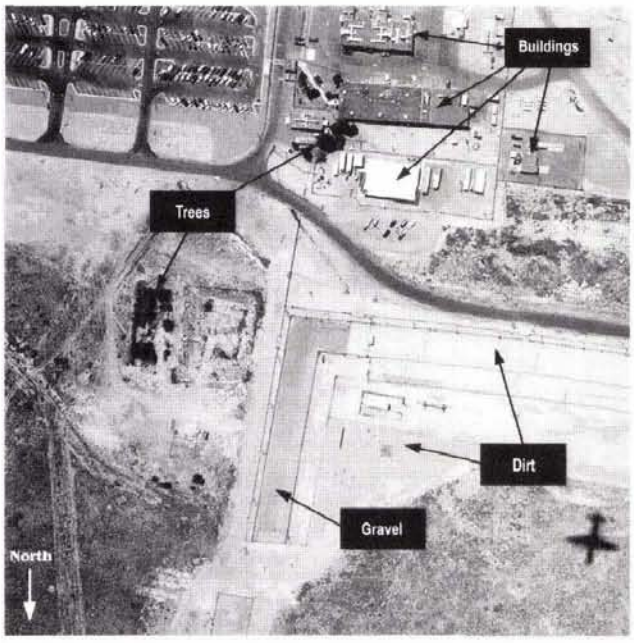

Figure 1. Overhead photograph of Sandia's Exterior Intrusion Sensor Facility, EISF, collected on 16 May 1996 by the Department of Energy's AMPS platform's Wild Heerbrugg RC-30 camera and digitized at about 0.6 m spatial resolution.

mately 0.6-m spatial resolution. The EISF contains gravel in the one arm of the "L," dirt in the other arm, and is surrounded by bare earth. To the east is a small depression with trees. To the south is a building complex also with trees. Southeast of the EISF is a parking lot.

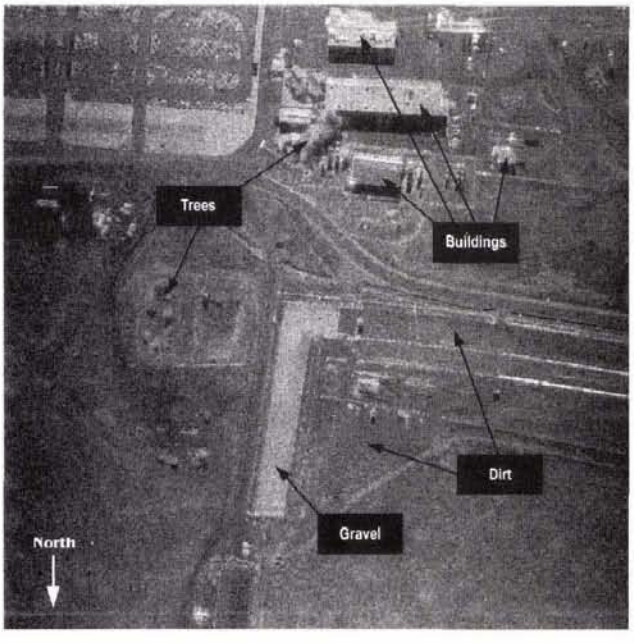

Figure 2. IFSAR magnitude imagery of the EISF at 0.37 m spatial resolution for pass 1 using antenna 1.

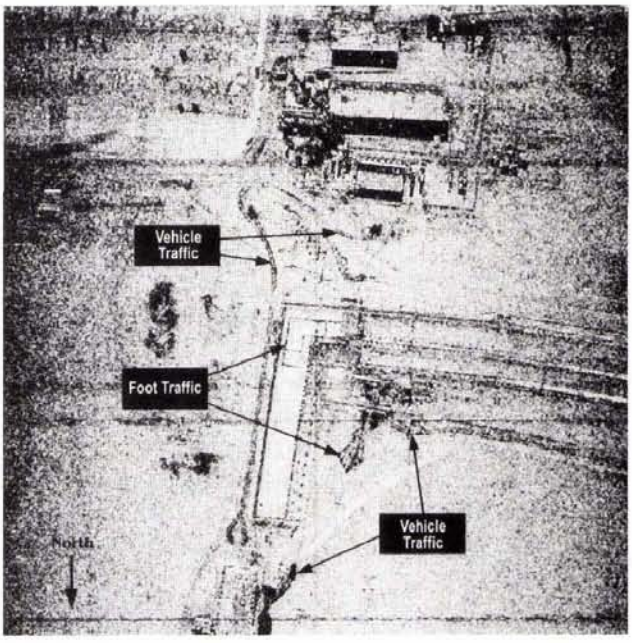

Figure 3. Interferometric change-detection, ICD, map of the EISF processed using a 5 by 5 correlation box.

Figure 2 is a SAR image of the EISF from the first pass of the collection using antenna 1. Near-range is the top of the figure. The EISF fence-line and hard returns from building structures are the prominent features. The gravel in the EISF as well as around the parking lot southeast of the EISF is brighter than the surrounding dirt and asphalt.

The ICD map in Figure 3 was processed using antenna 1 complex images from the selected passes with $i, j = 5$ (Equation 1), giving a 1.525-m resultant spatial resolution. The arrow-like feature in the dirt and polygons made in the EISF gravel are apparent. The tire tracks of vehicles traveling outside of the EISF fence-line are other decorrelated features. However, there are many other decorrelated pixels for which change "activities" are unknown.

Assume all temporal change activity is unknown. Experience may or may not help select the human and vehicle traffic as significant temporal changes in Figure 3. What quantitative approach can be used, in general, to interpret the ICD map? A correlation threshold can be chosen to identify significant change pixels. For our data, 31 percent (1,004,090 pixels) of the ICD map (1800 by 1800 pixels) has correlation of 80 percent or less. These pixels are identified as definite change and initially assumed to be temporal change.

The threshold levels we used in the following thermal, coherence, and height cases are consistent with the change level selected in the original ICD map (0.80). The magnitude threshold is *ad hoc*.

Signal-to-Noise/Thermal

The antenna pattern (the drop in SAR intensity due to the limited extent of antenna illumination over the aperture), shadows, and poor signal-to-noise can be addressed using the detected images and the magnitude of the signals. A simple approach is to assume a constant scene noise level and pick a low-signal threshold. We don't know the actual value for SNR, so we averaged over a 20- by 20-pixel area in a SAR shadow to find the noise level. Given this value and Equation 4, we used an SNR of 4.0 as the threshold for a 0.80 cor-

TABLE 1. THE NUMBER OF PIXELS IDENTIFIED AS FALSE TEMPORAL CHANGE BY DIFFERENT IFSAR-DERIVED CORRELATION PRODUCTS AND THEIR ACCUMULATED AMOUNTS

Correction Component	Number of Pixels	Accumulated Corrected Pixels
$\gamma_{thermal}$	390,530	390,530
$\gamma_{coherence}$	591,850	673,206
Magnitude	111,944	716,399
Terrain	42,950	744,881

relation value. Table 1 documents the number of pixels affected.

IFSAR Coherence

The coherence map for pass 1 is shown in Figure 4. Multiplying the coherence values from the two passes and then taking the square-root gives an estimate of the dual-pass thermal and spatial correlation. A 0.80 coherence threshold value was chosen for comparison with the ICD map "change" pixels. The resulting thresholded coherence pixels encompass 79 percent of the dual-pass thermal component estimate given above. This is not unexpected because the coherence comprises both spatial and thermal coherence components. For our case, one can use the coherence threshold instead of the above thermal threshold and still identify more false-change pixel candidates. As will be shown, it is the most important correction information we used. The results are shown in Table 1.

Magnitude Changes

For the case of identifying change due to light vehicles and human traffic, one would not see magnitude differences between image pairs in the disturbed areas. However, in cases where water has moistened the ground between data collections, the SAR magnitude will change. Being interested in the vehicle and human traffic changes, magnitude changes of 80 percent or more were found. The results are shown in Table 1.

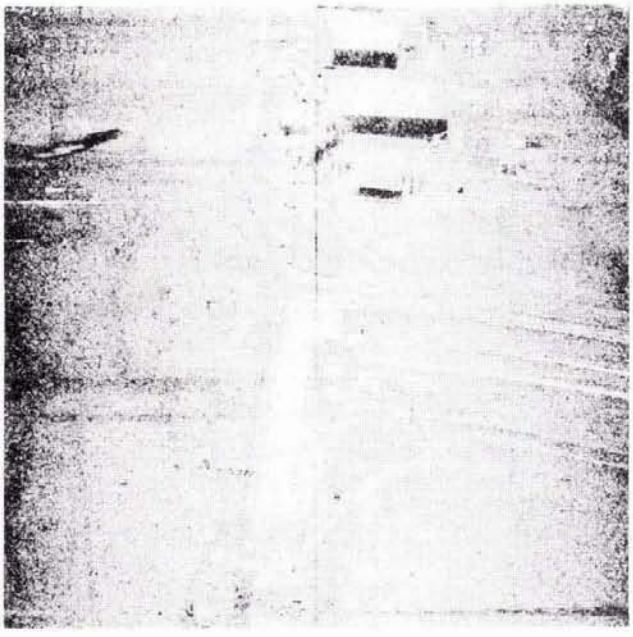

Figure 4. IFSAR coherence map for pass 1 over the EISF.

Height Map

The two-antenna AMPS IFSAR data are used to create height maps. Dual-pass SAR collections, like those for ICD maps, can also generate height maps. In either case, height maps are derived from the phase differences between the two collected signals. A height map can be very useful for sifting through the apparent changes. With ancillary information, such as interest in only ground-level changes, a height map will allow the elimination of buildings, fences, trees, and other features with relief. However, using the dual-pass ICD data pair for creating a height map may prove self-defeating because the decorrelations may or may not give reliable relative height values. In comparison, single-pass IFSAR height maps will not suffer from the dual-pass decorrelation, but they usually have smaller baselines, giving larger overall height noise. Stereo and historical height maps provide alternative information sources.

We used the dual-pass data pair to produce a height map of the test site because the single-pass height maps were comparatively noisy, and some height features were lost. Due to the phase unwrapping algorithm used (Ghiglia and Romero, 1994), the height map size is 1024 by 1024, a subset of the ICD map. Using Equation 5 and mission parameters $\phi = 35°$, $\rho_r = 0.3048$ m, $\lambda = 0.0200$ m, and $\Delta\phi = 0.00116$ radians, we solve for the local slope causing decorrelation of 0.80 or greater. Angles of 50.5° or greater satisfy this criterion. Slopes of this magnitude or greater were identified in the height map and the selected pixels dilated to 5- by 5-pixel areas, duplicating the ICD map resolution. Results are presented in Table 1.

Processing Results

All contributing false-change pixel locations were accumulated using a logical OR operation. These pixel locations were compared to the original low correlation ICD pixels. If coincident, the low correlation values were replaced with a 1.00 correlation value. The final ICD map is shown in Figure 5. Seventy-four percent of the original ICD decorrelations were identified as false changes. Although we identify non-temporal change and replace the values with 1.00 correlation, the correlation could also be estimated using the given components and applying a correction by solving Equation 3 for $\gamma_{temporal}$.

The thermal and coherence post-processing components identify the majority of the false changes. Their contributions are not independent. The coherence identifies 58.9 percent and the thermal 38.9 percent of the false change independently, but 67 percent collectively. If only one component could be used, the coherence would be the choice. The IFSAR coherence provides 20 percent more false-change detections than does the dual-pass SAR thermal component, showing the utility of IFSAR data in ICD map false-change identification post-processing. The SAR data by itself would identify 49 percent of the changes as false versus 59 percent using the IFSAR coherence alone. Using the IFSAR coherence instead of the SAR thermal correlation component increases the false-change identification to 68 percent, as shown by comparing Tables 2 and 3.

Figure 5 shows trees, buildings, shadows, and antenna pattern are well-corrected, leaving the human and vehicle traffic changes untouched. The identification of non-temporal decorrelation changes reduces the confusion produced by other decorrelating effects, assisting the user to focus on true temporal changes. Fences and some changes around the building areas are not identified completely. However, the building areas were not controlled for change in the experiment. The chain-linked fences change reflectances from pass to pass because of the inexact repeat geometry of the SAR. The height correction should have identified most of the dual-

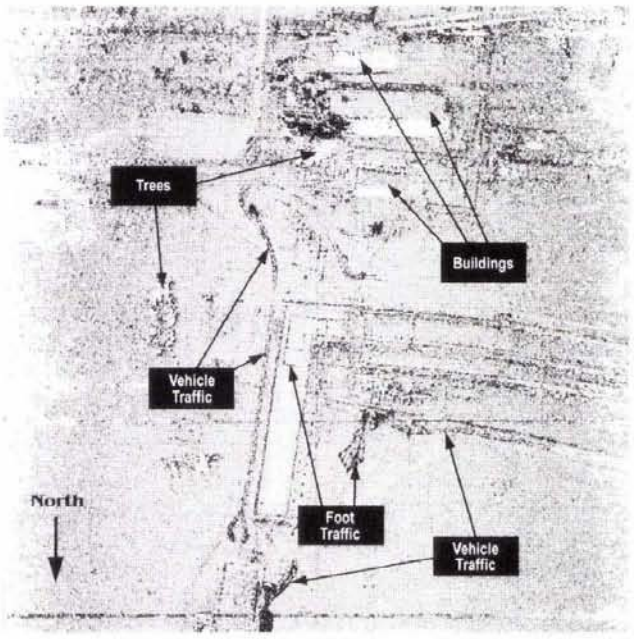

Figure 5. Post-processed result of Figure 3. False-change decorrelations of values less than 0.80 are set to correlation values of 1.0. Seventy-four percent of the original pixels designated as change were decorrelated due to system and target effects other than temporal change.

pass fence decorrelations, but the height data were noisy for the fence areas, resulting in few false-change identifications.

Future Directions

The corrections discussed above are derived from the SAR/IFSAR signal only. There are other options if other sensors are coresident on the platform. The AMPS platform has such coresident sensors. Spectral sensors can collect data within a few minutes of the SAR data. This near-simultaneous collection provides a multi-sensor snap-shot of the target. The addition of the multi-wavelength imagery data in conjunction with the ICD map may further reduce "false" change information. Vegetation decorrelation is one area in which this approach would be useful.

TABLE 2. THE NUMBER OF PIXELS IDENTIFIED AS FALSE TEMPORAL CHANGE BY SINGLE-ANTENNA SAR CORRELATION PRODUCTS AND THEIR ACCUMULATED AMOUNTS

Correction Component	Number of Pixels	Accumulated Corrected Pixels
$\gamma_{thermal}$	390,530	390,530
Magnitude	111,944	455,361
Terrain	42,950	486,849

TABLE 3. THE NUMBER OF PIXELS IDENTIFIED AS FALSE TEMPORAL CHANGE AND THEIR ACCUMULATED AMOUNTS WHEN EXCLUDING THE SAR THERMAL CORRELATION COMPONENT

Correction Component	Number of Pixels	Accumulated Corrected Pixels
$\gamma_{coherence}$	591,850	591,850
Magnitude	111,944	650,607
Terrain	42,950	681,441

Conclusions

Post-processing of ICD maps can greatly reduce apparent temporal changes by identifying false changes. A very good correction can be applied by using only IFSAR information, the single most important correction being the IFSAR coherence maps. The IFSAR coherence map gives a snap-shot of coherence values for each pass. Low coherence in one or each single-pass IFSAR complex data set is not indicative of long-term temporal change, and the resulting decorrelation can be tagged as no change.

Single-channel SAR data provided additional correction capability. In our case of combining both IFSAR and SAR data products, the false-change reduction was 74 percent of the original temporal change class. The amount of false-change reduction is dependent on phenomena captured by the image pairs.

Acknowledgments

The authors thank Mary Hoffman for processing the initial SAR images and Robert Huelskamp, AMPS project leader. This work was performed at Sandia National Laboratories under program funding for AMPS by Department of Energy's Office of Nonproliferation and National Security, and data exploitation by Department of Energy MIPR LR 603797, and Defense Special Weapons Agency under HD 11026244009. This work was also supported by the United States Department of Energy under Contract DE-AC04-94AL85000. Sandia is a multiprogram laboratory operated by Sandia Corporation, a Lockheed Martin Company, for the United States Department of Energy.

References

Askne, J.I.H., P.B.G Dammert, L.M.H. Ulander, and G. Smith, 1997. C-Band Repeat-Pass Interferometric SAR Observations of the Forest, *IEEE Trans. on Geoscience and Remote Sensing*, 35(1):25–35.

Bickel, D.L., and W.H. Hensley, 1996. *Design, Theory, and Applications of Interferometric Synthetic Aperture Radar for Topographic Mapping*, Sandia Report SAND96-1092.

Eichel, P.H., D.C. Ghiglia, C.V. Jakowatz, P.A. Thompson, and D.E. Wahl, 1996. *Spotlight SAR Interferometry and Interferometric Change Detection*, Sandia Report SAND93-2072.

Gabriel, A.K., R.M. Goldstein, and H.A. Zebker, 1989. Mapping Small Elevation Changes Over Large Areas: Differential Radar Interferometry, *J. Geophys. Res.* 90(B7):9183–9191.

Ghiglia, D.C., and L.A. Romero, 1994. Robust Two-Dimensional Weighted and Unweighted Phase Unwrapping that Uses Fast Transforms and Iterative Methods, *J. Opt. Soc. Amer. A*, 11(1): 107–117.

Goodman, J.W., 1985. *Statistical Optics*, John Wiley & Sons, New York.

Gray, A.L., and P.J. Farris-Manning, 1993. Repeat-Pass Interferometry with Airborne Synthetic Aperture Radar, *IEEE Trans. on Geoscience and Remote Sensing*, 31(1):180–191.

Jakowatz, C.V., D.E. Wahl, P.H. Eichel, D.C. Ghiglia, and P.A. Thompson, 1996. *Spotlight-Mode Synthetic Aperture Radar: A Signal Processing Approach*, Kluger Academic, Boston.

Massonnet, D., M. Rossi, C. Carmona, F. Adragna, G. Peltzer, K. Feigl, and T. Rabaute, 1993. The Displacement Field of the Landers Earthquake Mapped by Radar Interferometry, *Nature*, 364: 138–142.

Prati, C., 1989. 3-D Synthetic Aperture Radar Surveys, *Proceedings of the IEEE International Conference on Acoustics, Speech, and Signal Processing*, pp. 2376–2379.

Rodriguez, E., and J.M. Martin, 1992. Theory and Design of Interferometric Synthetic Aperture Radars, *Proc. Inst. Elec. Eng.*, Pt F, 139(2):147–159.

Zebker, H.A., and J. Villasenor, 1992. Decorrelation in Interferometric Radar Echoes, *IEEE Trans. on Geoscience and Remote Sensing*, 30(5):950–959.

(Received 22 May 1997; accepted 25 September 1997; revised 5 November 1997)